Miner Deposita (2017) 52:495–514
DOI 10.1007/s00126-016-0674-8

ARTICLE

Role of evaporitic sulfates in iron skarn mineralization: a fluid inclusion and sulfur isotope study from the Xishimen deposit, Handan-Xingtai district, North China Craton

Guang Wen[1,2] · **Shi-Jian Bi**[2] · **Jian-Wei Li**[1,2]

Received: 24 July 2015 / Accepted: 18 July 2016 / Published online: 18 August 2016
© Springer-Verlag Berlin Heidelberg 2016

Abstract The Xishimen iron skarn deposit in the Handan-Xingtai district, North China Craton, contains 256 Mt @ 43 % Fe (up to 65 %). The mineralization is dominated by massive magnetite ore along the contact zone between the early Cretaceous Xishimen diorite stock and middle Ordovician dolomite and dolomitic limestones with numerous intercalations of evaporitic beds. Minor lenticular magnetite-dominated bodies also occur in the carbonate rocks proximal to the diorite stock. Hydrothermal alteration is characterized by extensive albitization within the diorite stock and extreme development of magnesian skarn along the contact zone consisting of diopside, forsterite, serpentine, tremolite, phlogopite, and talc. Magmatic quartz and amphibole from the diorite and hydrothermal diopside from the skarns contain abundant primary or pseudosecondary fluid inclusions, most of which have multiple daughter minerals dominated by halite, sylvite, and opaque phases. Scanning electron microscopy (SEM) and laser Raman spectrometry confirm that pyrrhotite is the predominant opaque phase in most fluid inclusions, in both the magmatic and skarn minerals. These fluid inclusions have total homogenization temperatures of 416–620 °C and calculated salinities of 42.4–74.5 wt% NaCl equiv. The fluid inclusion data thus document a high-temperature, high-salinity, ferrous iron-rich, reducing fluid exsolved from a cooling magma likely represented by the Xishimen diorite stock. Pyrite from the iron ore has $\delta^{34}S$ values ranging from 14.0 to 18.6 ‰, which are significantly higher than typical magmatic values ($\delta^{34}S = 0 \pm 5$ ‰). The sulfur isotope data thus indicate an external source for the sulfur, most likely from the evaporitic beds in the Ordovician carbonate sequences that have $\delta^{34}S$ values of 24 to 29 ‰. We suggest that sulfates from the evaporitic beds have played a critically important role by oxidizing ferrous iron in the magmatic-hydrothermal fluid, leading to precipitation of massive magnetite ore. A synthesis of available data suggests that oxidation of Fe^{2+}-rich, magmatic-hydrothermal fluids by external sulfates could have been a common process in many of the world's iron skarn deposits and other magnetite-dominated ores, such as iron oxide-copper-gold (IOCG) and iron oxide-apatite (IOA) systems.

Introduction

Evaporitic rocks widely occur in a variety of geological environments and have close spatial relationships with several major types of iron oxide-rich ores, such as iron oxide copper and gold (IOCG) and iron oxide-apatite deposits (IOA) (Cai 1981; Barton and Johnson 1996, 2000; Hitzman 2000; Chen 2013; Li et al. 2015). Previous studies have shown that evaporites may have significantly facilitated transport of iron in hydrothermal fluids by providing sufficient amounts of chlorine to form iron-chloride complexes (Zhao et al. 1990; Barton and Johnson 1996, 2000).

It is commonly thought that iron is present predominantly as ferrous iron (Fe^{2+}) in magmatic-hydrothermal systems (Crerar and Barnes 1976; Barnes 1979; Simon et al. 2013). In this case, the formation of voluminous iron oxides requires sufficient oxidation of Fe^{2+} to Fe^{3+}. However, the mechanisms by which this oxidation process takes place are not well understood. Eugster and Chou (1979) proposed that O_2 produced by

Editorial handling: S.-Y. Jiang

✉ Jian-Wei Li
jwli@cug.edu.cn

[1] State Key Laboratory of Geological Processes and Mineral Resources, China University of Geosciences, Wuhan 430074, China

[2] Faculty of Earth Resources, China University of Geosciences, Wuhan 430074, China

dissociation of H_2O may be responsible for the oxidation of ferrous iron and, consequently, precipitation of hydrothermal magnetite. However, the amount of O_2 would be insufficient to maintain the abovementioned oxidation reaction if H_2 derived from the dissociation of H_2O is not efficiently removed from the reacting system (Takagi and Tsukimura 1997). Thus, an alternative mechanism must be considered to adequately explain the formation of voluminous iron oxides in magmatic-hydrothermal systems.

Iron skarns are among the largest known skarn deposits, with many containing several hundred million tons of iron metal (Meinert et al. 2005 and references therein). The ores are typically dominated by magnetite with variable amounts of associated silicate minerals such as garnet and diopside, which formed as a result of hydrothermal metasomatism between magmatic-hydrothermal fluids and marine carbonate rocks (Einaudi 1981; Meinert 1984; Meinert et al. 2005). Iron skarn-related magmas are considered to have lower oxygen fugacities relative to the varieties associated with Cu, Mo, and Zn skarn deposits (Meinert 1995; Meinert et al. 2005). The low-oxygen fugacities of the parent magmas indicate that sulfides, rather than sulfates, may have been the major sulfur species in the magmatic-hydrothermal systems, and consequently, iron is likely to have been present mainly as Fe^{2+}. In this case, voluminous magnetite precipitation would be unlikely without oxidation of the ferrous iron by external oxidants.

Iron skarn deposits have been the most important source of high-grade iron ores (>55 % total Fe) in China since their discovery in the early 1900s (Zhao et al. 1990). The Daye, Handan-Xingtai, Linfen, and Laiwu districts in eastern China host the largest concentrations of iron skarn deposits in the country (Fig. 1). All these iron ore districts are characterized by widespread evaporites within Paleozoic or early Mesozoic marine carbonate sequences into which the ore-related plutonic bodies were emplaced. Field relationships and sulfur isotopic compositions (e.g., Yuan 1982; Cai et al. 1987; Zhang et al. 2013a; Hu et al. 2014; Xie et al. 2015) indicate that evaporites may have been critically important in the formation of those high-grade iron skarn deposits. However, how the evaporates have contributed to the large-scale iron skarn mineralization remains poorly understood. In this paper, we present fluid inclusion and sulfur isotope data of the Xishimen iron skarn deposit from the Handan-Xingtai district (Fig. 2), the second largest producer of high-grade iron ore in China to characterize the nature of the ore-forming fluids and to demonstrate the important role of evaporites as an efficient oxidant in iron skarn mineralization throughout the district. We further compile data from other localities of the world to suggest that oxidation of ferrous iron by external sulfates may have been a common process in the formation of many iron oxide-dominated ores such as IOCG and IOA.

Geological setting

The Handan-Xingtai district is located within the Trans-North China Orogen, which formed at ca. 1.85 Ga due to continental collision between the Western and Eastern Blocks of the North China Craton (NCC) that resulted in final amalgamation and stabilization of this craton (Zhao et al. 2005; Fig. 1). The basement of the NCC consists of Archean to Paleoproterozoic TTG gneisses and subordinate mafic granulites and amphibolites.

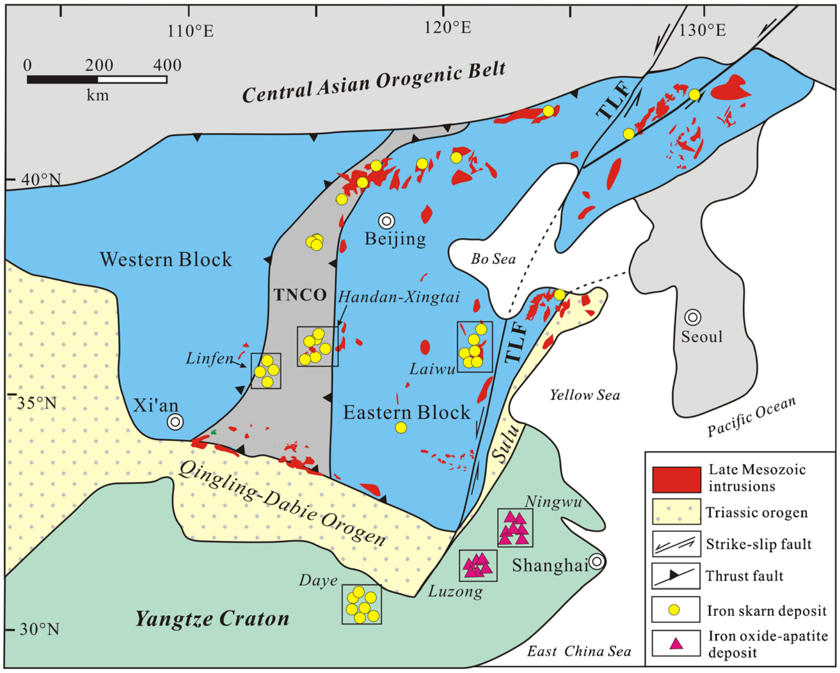

Fig. 1 A simplified map showing the tectonic divisions of the North China Craton and adjacent regions. Also shown is the distribution of late Mesozoic intrusions and major districts hosting large iron skarn and iron oxide-apatite deposits (modified from Zhao et al. 2005; Li et al. 2012; Jin et al. 2015). *TLF* Tan-Lu Fault, *TNSO* Trans North China Orogen

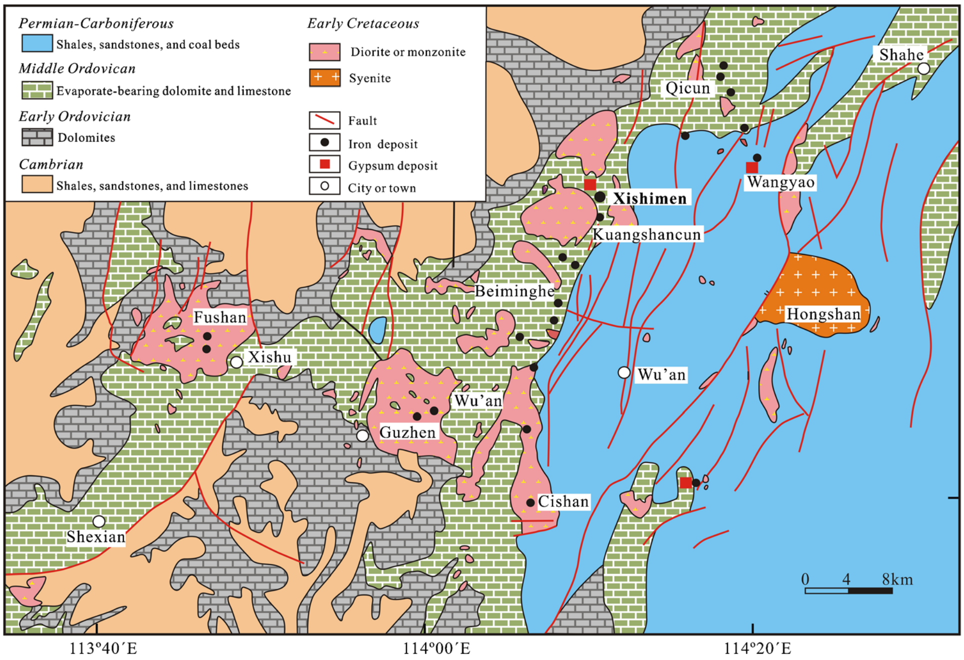

Fig. 2 Geological map of the Handan-Xingtai district showing the distribution of major iron skarn deposits and gypsum deposits (Li et al. 2013b; IGSNC 1976)

From the late Paleoproterozoic to the end of the Paleozoic, the NCC was tectonically stable and received relatively continuous deposition of shallow-marine carbonate platform sediments (Yang et al. 1986).

In the Handan-Xingtai district, the Precambrian basement is overlain unconformably by about 3500 m of Paleozoic (Cambrian to Permian) marine sedimentary rocks (Zheng 2007). The Cambrian strata consist of limestones, sandstones, and shales, which are conformably overlain by early Ordovician dolomites. Middle Ordovician strata conformably overlie the early Ordovician dolomites and consist chiefly of evaporite-bearing carbonates, which host numerous economic

Fig. 3 Lithostratigraphic components of middle Ordovician strata in the Handan-Xingtai district (modified from Cai et al. 1987)

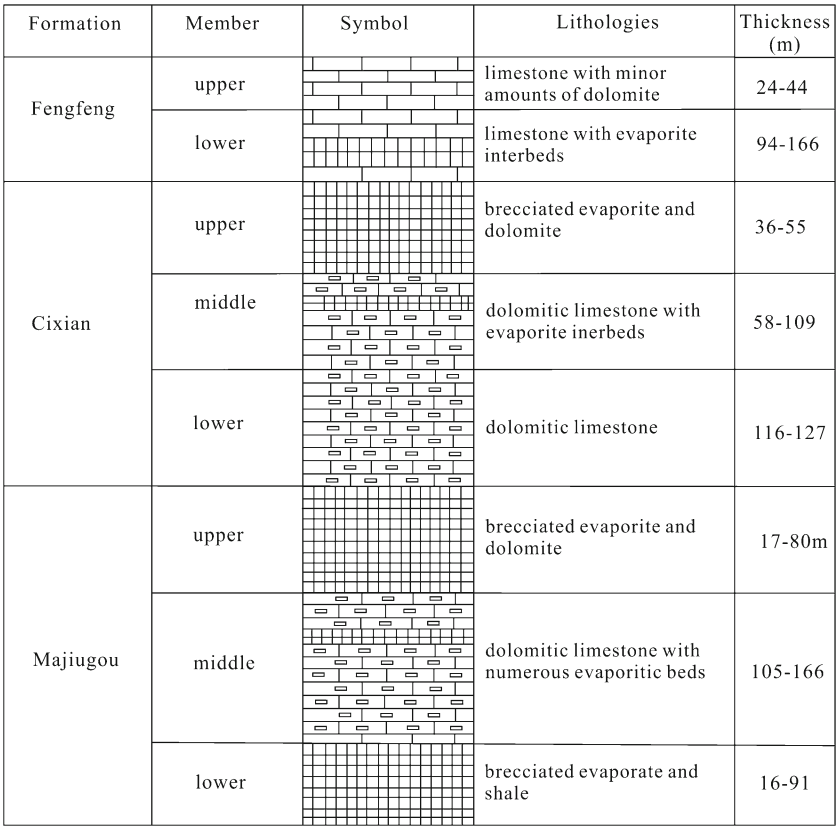

Formation	Member	Symbol	Lithologies	Thickness (m)
Fengfeng	upper		limestone with minor amounts of dolomite	24-44
	lower		limestone with evaporite interbeds	94-166
Cixian	upper		brecciated evaporite and dolomite	36-55
	middle		dolomitic limestone with evaporite inerbeds	58-109
	lower		dolomitic limestone	116-127
Majiugou	upper		brecciated evaporite and dolomite	17-80m
	middle		dolomitic limestone with numerous evaporitic beds	105-166
	lower		brecciated evaporate and shale	16-91

gypsum deposits (Cai et al. 1987). More than 95 % of the total iron reserves in the Handan-Xingtai district are hosted by the middle Ordovician sequence (Fig. 2). The middle Ordovician strata can be divided, from the base upward, into the Majiagou, Cixian, and Fengfeng Formations (Fms.; Fig. 3). The 140- to 344-m-thick Majiagou Fm. is composed of shales and evaporites in its lower member, dolomites, dolomitic limestones, and interbedded evaporites in the middle member and brecciated evaporites and dolomites in the upper member. The Cixian Fm., with a total thickness of 186–343 m, is also divided into lower, middle, and upper members, which are dominated by dolomitic limestones with many evaporite intercalations and brecciated evaporites with minor amounts of dolomite, respectively. The Fengfeng Fm. consists of 118–210 m of dolomitic limestones and multiple evaporitic beds in a lower member and limestones in an upper member (Fig. 3). Dissolution breccias are widespread in the middle Ordovician sequence wherever evaporitic beds are present. The Carboniferous to Permian sequences, which mainly crop out in the eastern part of the Handan-Xingtai district, are dominated by shales, coal beds, and sandstones that unconformably overlie the middle Ordovician rocks.

The Paleozoic sedimentary rocks are intruded by several major plutons and numerous smaller stocks, ranging in composition from diorite to monzonite and syenite. These intrusions form three NNE-trending magmatic belts, locally called the Fushan, Wu'an, and Hongshan belts (Fig. 2). Iron deposits in the district are restricted to the Fushan and Wu'an belts, but no economic iron ores have been discovered within the Hongshan belt. Recent zircon U-Pb geochronological studies have shown that the granitic intrusions throughout the Handan-Xingtai district formed at 136–135 and 132–130 Ma (Peng et al. 2004;

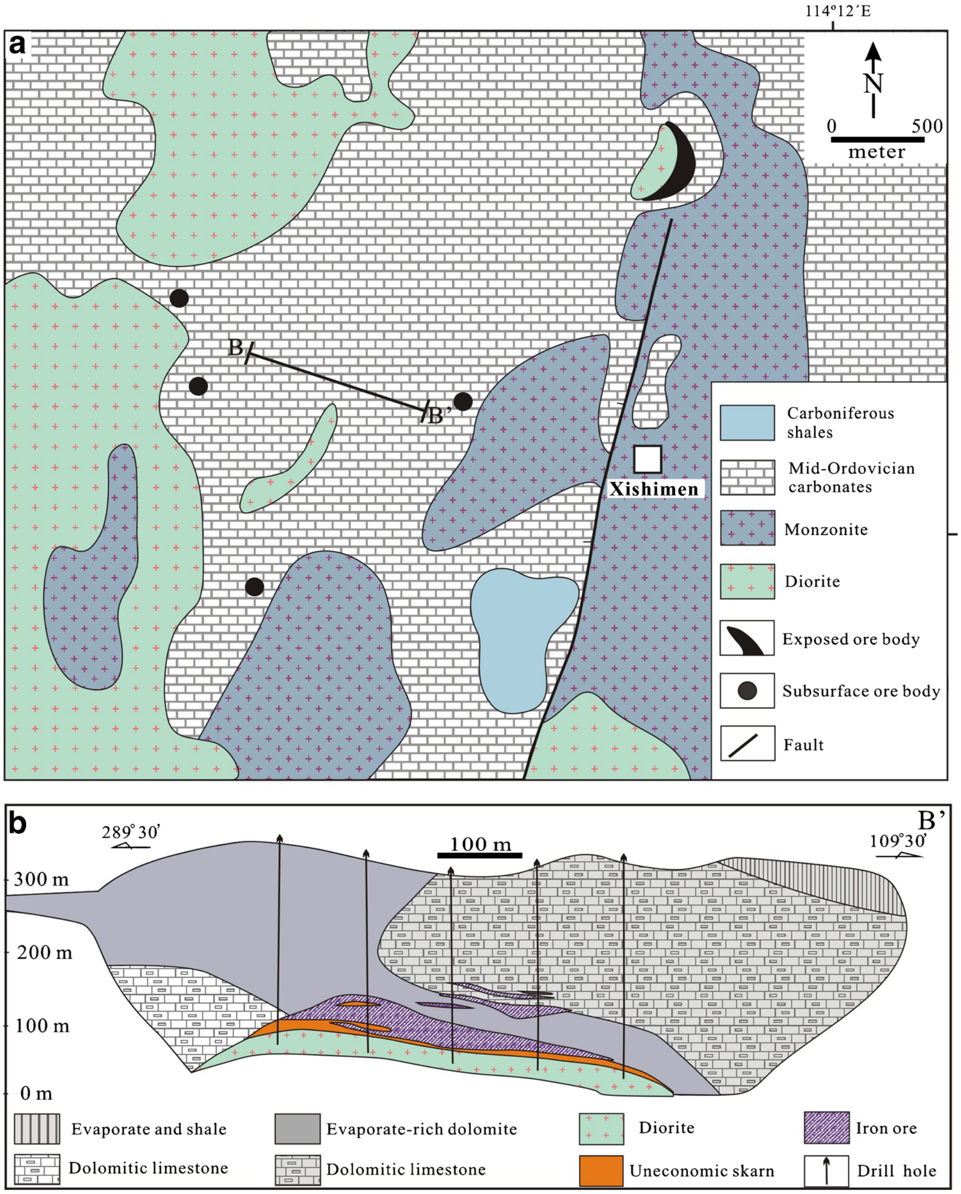

Fig. 4 Geological map (**a**) and the no. 5 section (**b**) of the Xishimen iron skarn deposit (Zhang and Ma 1996; Zhang et al. 2013b; Cai et al. 1987)

Chen et al. 2008; Shen et al. 2012; Li et al. 2013a; Sun et al. 2014; Deng et al. 2015). These early Cretaceous magmatic rocks are interpreted to have resulted from mixing of lower crustal- and metasomatized mantle-derived melts in response to thinning and destruction of the mantle lithosphere beneath the NCC, a process ultimately triggered by subduction of the paleo-Pacific plate underneath the eastern China continental margin (Li et al. 2012; Shen et al. 2012).

The Xishimen iron skarn deposit

The Xishimen iron skarn deposit is situated in the middle of the Wu'an magmatic belt and has a proven resource of 256 Mt @ 35–65 % Fe (HGI 1984). Mineralization occurs predominantly along the contact zone between the Xishimen diorite stock and the upper member of the middle Ordovician Majiagou Fm., which is dominated by dolomite with numerous evaporite intercalations (Fig. 4). Minor amounts of iron ore are hosted within the upper member of the Majiagou and lower member of the Cixian Fms. in close proximity to the Xishimen diorite intrusion (Fig. 4). Logging of diamond drill core has revealed six to nine gypsum-dominated evaporitic beds in the upper member of the Majiagou Fm., individually 5 to 50 m in thickness (Cui 1983).

The Xishimen diorite has a medium-grained texture and consists of plagioclase (50–70 vol%), hornblende (10–25 vol%), K-feldspar (10–15 vol%), and quartz (5–7 vol%). The rocks contain 58.5–59.8 wt% SiO_2, 16.0–16.6 wt% Al_2O_3, 2.02–2.79 wt% MgO, 4.88–8.20 Na_2O, 0.28–3.23 K_2O, 4.70–6.65 CaO, and 4.77–6.93 wt% FeO^{total}, with high $Mg^{\#}$ of 46–47 and low A/CNK values of 0.64–0.65 (Wei 2011). They are enriched in large-ion lithophile elements (e.g., Sr, Ba, Th, K) and depleted in high-field-strength elements (e.g., Nb and Ti) and are characterized by strong fractionation between light rare earth element (REE) and heavy REE but lack obvious Eu anomalies (Wei 2011). Laser ablation ICP-MS dating of zircon from a fresh diorite sample yielded a concordant U-Pb age of 134 ± 1 Ma (Li et al. 2013a). Available geochemical and isotope data indicate that the Xishimen diorite was likely derived from partial melting of late Archean lower crust, followed by fractional crystallization during magma ascent (Wei 2011).

The Xishimen iron skarn deposit consists of 28 ore bodies, most of which are unexposed and occur at between 10 and 474 m below the present surface as revealed by diamond drilling (IGSNC 1976, Fig. 4b). The main ore body accounts for >95 % of the total iron reserves and is dominated by massive magnetite-rich ores (>50 % Fe). It is about 5020 m long, 125 to 1076 m wide, and 1.2 to 103.5 m thick. Skarn assemblages are poorly developed, but sulfide minerals, dominated by pyrite as disseminations or veins, are abundant in the iron ores (Fig. 5a). Pyrite is also present as massive aggregates and veins within the limestone of the Majiagou Fm. distal to the orebodies. Hematite-magnetite ores are well developed in brecciated marble with very thin or no alteration halos.

On the basis of field and textural relationships, three hydrothermal alteration assemblages are recognized, including albitization, prograde skarn, and retrograde skarn assemblages. Albitization is extensive and mostly developed in the upper part of the Xishimen diorite, where plagioclase is typically replaced by albite and/or epidote, whereas hornblende is altered to form albite and diopside. Diopside-albite veinlets, generally 1–5 cm wide, are particularly abundant near the endoskarn. Prograde skarn assemblages are well developed

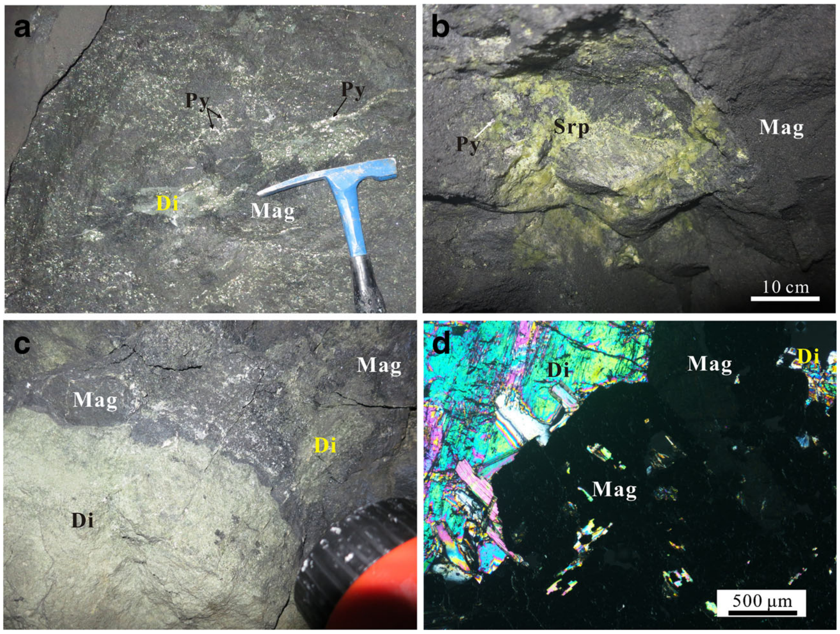

Fig. 5 Field photographs and microphotographs showing hydrothermal alteration and magnetite-dominated ores in the Xishimen iron deposit. **a** Pyrite in magnetite ore. **b** Massive magnetite coexisting with serpentine and pyrite. **c** Magnetite veins overprinting diopside skarn. **d** Transmitted light photomicrograph showing magnetite texturally associated with diopside. *Di* diopside, *Mag* magnetite, *Srp* serpentine, *Py* pyrite

in the endoskarn zone but are rare in the exoskarn zone and the magnetite ores. The prograde skarns consist of >80 % diopside, ranging from 0.2 to 20 mm in size, with minor forsterite and albite. In most cases, magnetite mineralization postdates the prograde skarn minerals (Fig. 5c, d). The retrograde skarn alteration is most extensive within the exoskarn zone and is closely associated with magnetite ores. Predominant retrograde skarn minerals include serpentine, tremolite, talc, chlorite, and phlogopite (Fig. 5b).

A phlogopite separate from a massive magnetite ore yielded an $^{40}Ar/^{39}Ar$ plateau age of 133.1 ± 1.3 Ma (Zheng et al. 2007), which is marginally consistent with a zircon U-Pb age of 134 ± 1 Ma for the Xishimen diorite (Li et al. 2013a). The age consistency indicates a temporal and possibly genetic relation between the diorite intrusion and magnetite mineralization. This view is confirmed by a more recent study that yields U-Pb age of 134.1 ± 1.2 Ma for hydrothermal zircon from an iron mineralized exoskarn and 133.6 ± 0.9 Ma for magmatic zircon from the Xishimen diorite (Deng et al. 2015).

Samples and analytical methods

Fluid inclusion study

Ten fresh diorite samples and ten mineralized diopside skarn samples were collected from underground works at 200 to 400 m below the present surface for fluid inclusion petrographic study. Polished thin sections (~100 μm thick) of each sample were examined under transmitted light to identify the shape, size, distribution, and phases of fluid inclusions. Microthermometric measurements were then made using a Linkam THMS-600 heating-freezing stage, which was calibrated using synthetic inclusions distributed by Fluid Inc., USA. Uncertainties of the measurements were ±2 °C for runs in the range of 100 to 600 °C. The heating/freezing rate was generally 1 to 5 °C/min but was reduced to less than 1 °C/min near the phase transformations. Fluid inclusions with homogenization temperatures higher than 600 °C were carried out on a modified Leitz 1350 heating stage. The heating rate ranged from 2 to 10 °C/min but was reduced to less than 2 °C/min near the phase transformations. Uncertainties of the measurement were ±5 °C.

Daughter mineral-bearing fluid inclusions were further investigated using scanning electron microscopy and laser Raman spectroscopy. After petrographic examination, the thin sections were gently polished in kerosene until the inclusions were opened and the daughter minerals were exposed. The exposed daughter minerals were then analyzed using a JEOL Quanta-200 environmental scanning electron microscope (SEM) equipped with an energy-dispersive spectrometer (EDS). Laser Raman spectrometry was carried out on selected fluid inclusions using a Jobyn Yvon Horiba LabRam-IRHR 800 spectrometer equipped with a 532-nm Ar-ion laser as the source of excitation. The Raman spectra were acquired from 0 to 4000 cm^{-1} using a measured spectrum time of 30 s.

Sulfur isotope analysis

Eleven pyrite samples were collected from the main ore body at 210 to 250 m below the present surface, whereas two calcite-pyrite veins were taken from drill holes ZK57 and ZK18, respectively. After petrographic examination, the samples were crushed, washed in distilled water in an ultrasonic bath for at least 1 h, and dried. Pyrite separates were then handpicked under

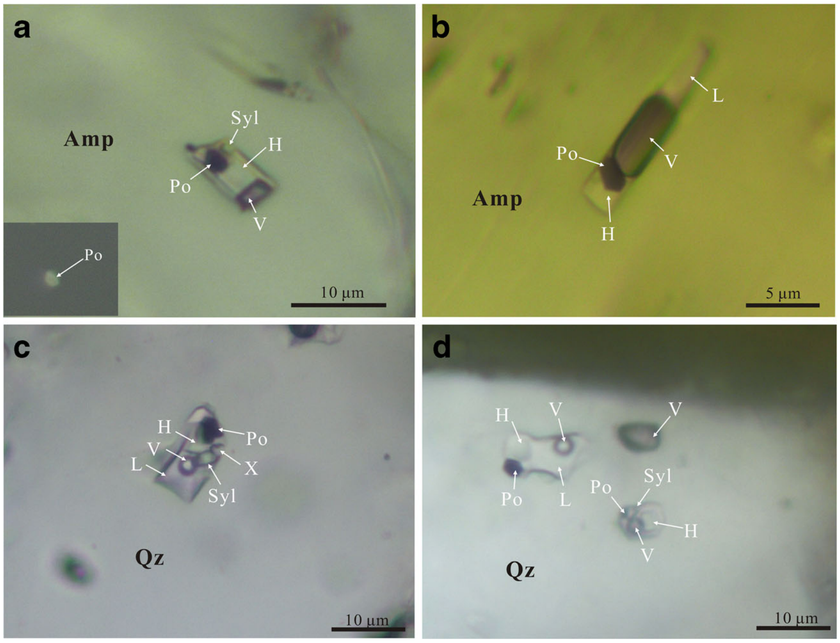

Fig. 6 Photomicrographs of fluid inclusions in igneous amphibole and quartz. **a** Fluid inclusion in amphibole containing multiple daughter minerals. The regular shape and *brownish gray reflection color* indicate that the opaque phase is likely pyrrhotite. **b** Halite- and opaque mineral-bearing fluid inclusion in amphibole. **c** Fluid inclusion in quartz containing multiple daughter minerals. **d** Opaque mineral-bearing fluid inclusions coexisting with vapor-rich fluid inclusion in quartz. *V* vapor phase, *L* liquid phase, *H* halite, *Syl* sylvite, *X* unidentified phase, *Po* pyrrhotite, *Amp* amphibole, *Qz* quartz

a binocular microscope. Whenever possible, coarse pyrite grains were targeted to minimize contamination by other minerals. Sulfur isotopic ratios were determined using a conventional off-line method. Approximately 15 mg of pyrite was homogenized with 150 mg of Cu_2O, combusted at 1050 °C for 15 min under vacuum for a quantitative conversion to sulfur dioxide (SO_2), which was then analyzed for sulfur isotopic compositions on a MAT 251 mass spectrometer. The results are reported in standard δ notation in ‰ relative to Canyon Diablo troilite (CDT). The reproducibility of $\delta^{34}S$ values was ±0.2 ‰.

Results

Fluid inclusions

Fluid inclusions are well developed both in magmatic quartz and amphibole from the diorite samples and in hydrothermal diopside from the skarn samples. Three types of fluid inclusions were distinguished based on their characteristics at room temperature, including two-phase, liquid-rich, aqueous inclusions (type 1), daughter mineral-bearing multiple phase inclusions (type 2), and two-phase, vapor-rich aqueous inclusions (type 3).

Fluid inclusions in magmatic amphibole and quartz

Amphibole hosts abundant type 2 fluid inclusions, occurring as cylindrical isolations typically 3–8 μm across (Fig. 6a, b). They are mostly distributed along the cleavage planes in the amphibole. Type 2 inclusions typically contain a vapor phase that accounts for 10 to 40 % of the total volume and have two to three daughter minerals consisting of halite, sylvite, and an opaque phase (Fig. 6a, b). The opaque mineral is euhedral to subhedral and commonly has a hexagonal shape. Its morphology and reflection color (brownish to grayish yellow) indicate that it is most likely pyrrhotite (inset of Fig. 6a), as partly confirmed by scanning electron microscopy combined with energy-dispersive spectrometry (SEM-EDS) and laser Raman spectroscopy (see below).

All three types of fluid inclusions are present in magmatic quartz from the diorite. Type 1 inclusions are small (<5 μm) and occur as trails penetrating crystal boundaries, features interpreted to be of secondary origin (Reodder 1984). Type 2

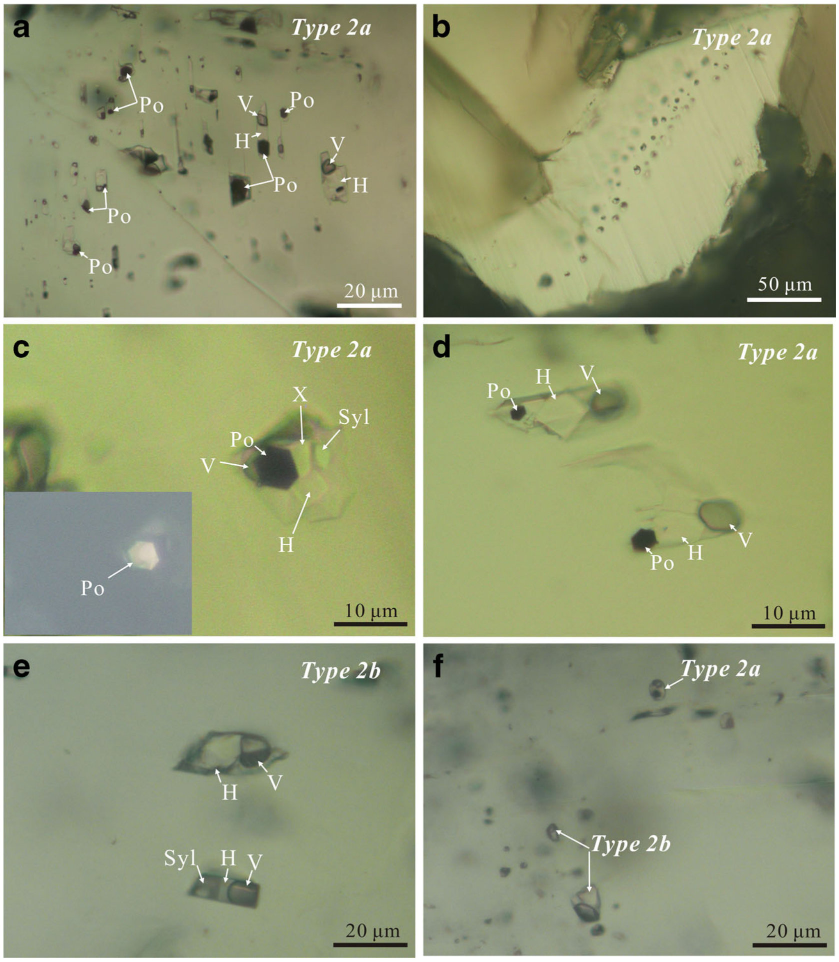

Fig. 7 Photomicrographs of daughter mineral-bearing fluid inclusions in diopside. **a** Opaque mineral-bearing fluid inclusions (type 2a) randomly distributed in diopside. **b** Pseudosecondary type 2a fluid inclusions (type 2a) in diopside. **c** *Brownish gray color* and regular hexagonal shape of an opaque mineral, most likely pyrrhotite. **d** Cylindrical opaque mineral-bearing fluid inclusions (type 2a) in diopside. **e** Type 2b fluid inclusions in diopside. **f** Coexisting type 2a and type 2b fluid inclusions in diopside. Mineral and phase abbreviations as in Figs. 5 and 6

fluid inclusions are subhedral to anhedral, 5–10 μm in diameter, and developed along growth zones of the host mineral (Fig. 6c, d). The solid phases in type 2 inclusions are dominated by halite and pyrrhotite, with or without sylvite. Type 3 inclusions, frequently coexisting with type 2 varieties, are 5 to 8 μm in size and have round to negative crystal shapes (Fig. 6d).

Fluid inclusions in diopside from skarns

Daughter mineral-bearing, multiple-phase fluid inclusions (type 2) are abundant in diopside and can be divided into two subtypes. Type 2a inclusions contain halite ± sylvite and an opaque phase, whereas type 2b varieties only have halite ± sylvite with no associated opaque daughter minerals. Type 2a fluid inclusions are the predominant variety and range in diameter from 10 to 30 μm. In most cases, they occur mostly as isolations or clusters (Fig. 7a) but are also present as trails within diopside crystals (Fig. 7b). The occurrence and distribution of the type 2a fluid inclusions indicate a primary or pseudosecondary origin (Reodder 1984). The identified solid phases are mainly halite and pyrrhotite, but some of these inclusions also contain sylvite (Fig. 7a–d). The vapor phase accounts for 10–30 % of the total volume of individual type 2a inclusions. Type 2b inclusions are less abundant and smaller (5–20 μm) and occur as subhedral to anhedral isolations (Fig. 7c, d). The vapor-rich type 3 inclusions are rare and less than 8 μm in size. Wherever present, they coexist with type 2 inclusions.

Microthermometry

Fluid inclusions in amphibole and quartz are not considered for subsequent microthermometric study due to their small size. A total of 71 microthermometric measurements were made on type 2a and 2b inclusions hosted in diopside. Salinities of fluid inclusions containing both halite and sylvite were determined by halite and sylvite dissolution temperatures, using the NaCl-KCl-H_2O diagram (Sterner et al. 1988). The microthermometric data are summarized in Table 1 and graphically illustrated in Figs. 8 and 9.

All type 2a inclusions showed similar microthermometric behavior, with vapor bubble disappearance followed by halite dissolution (Fig. 9). Vapor-liquid homogenization occurred in the range of 410–542 °C, but heating above 500 °C led to decrepitation of some inclusions. Sylvite and halite dissolution took place at temperatures of 230–310 and 420–578 °C, respectively. The salt dissolution temperatures yield calculated salinities of 49.7 to 70.8 wt% NaCl equiv. for halite-bearing inclusions and 63 to 74 wt% NaCl equiv. for halite- and sylvite-bearing inclusions (13–26 wt% KCl equiv. and 39–54 wt% NaCl equiv.; Fig. 8b). The opaque phases did not dissolve even after the heating temperature increased to 800 °C.

Type 2b fluid inclusions were homogenized to a liquid between 416 and 620 °C, either by halite dissolution or by vapor bubble disappearance. Halite dissolution and vapor bubble disappearance took place between 380 and 585 °C and between 408 and 620 °C, respectively (Fig. 8a). Sylvite dissolution occurred in the range of 185–280 °C, significantly prior to halite dissolution. The calculated salinities are 42.4–74.5 wt% NaCl equiv. (Fig. 8b). Within some assemblages, fluid inclusions homogenized to liquid by vapor and halite disappearance in a small temperature interval of 6° to 30 °C.

Scanning electron microscopy

SEM-EDS provides a powerful tool for the study of daughter minerals in opened fluid inclusions (Metzger et al. 1977). Using this tool, a variety of daughter minerals have been identified in opened type 2a and type 2b inclusions in diopside. Both halite and pyrrhotite are common in type 2a inclusions. The halite crystals typically have a cubic form and range from 2 to 15 μm in diameter (Fig. 10a–d). Pyrrhotite crystals occur at the base or along the margins of the exposed inclusions, commonly beneath or texturally associated with halite crystals (Fig. 10a–d). These pyrrhotite crystals are generally hexagonal and range from 1 to 7 μm in diameter. Sylvite crystals were locally observed, coexisting exclusively with halite whenever they occur (Fig. 10d). Halite is the major daughter mineral in type 2b inclusions (Fig. 10e, f) but is locally accompanied with cubic crystals of sylvite up to 5 μm in diameter.

Laser Raman spectroscopic analysis

Laser Raman spectroscopic analyses were performed on representative daughter mineral-bearing inclusions (type 2) in quartz of the diorite and the diopside of the skarn samples. Abundant pyrrhotite crystals have been identified in type 2 inclusions in both quartz and diopside based on Raman displacement peaks at 378 to 379 and 340 to 342 cm^{-1} (Fig. 11a, c), respectively, confirming results of the SEM-EDS analyses (Fig. 10). The vapor phase of type 2 inclusions in quartz and diopside is dominated by H_2O, variably with minor amounts of CO_2 (Fig. 11b, d).

Iron concentrations of type 2a fluid inclusions in diopside

Iron concentrations of the fluid inclusions were calculated using the phase volume method proposed by Kwak et al. (1986). The concentrations are expressed as follows: Fe (wt%) = $V_{\mathrm{Po}} * \rho_{\mathrm{Po}} * 60\ \% / (V_{\mathrm{Po}} * \rho_{\mathrm{Po}} + V_{\mathrm{Hl}} * \rho_{\mathrm{Hl}} + V_{\mathrm{liquid}} * \rho_{\mathrm{liquid}})$, where $V_{\mathrm{Po}} * \rho_{\mathrm{Po}}$ indicates the mass of

Table 1 Microthermometric data of fluid inclusions in diopside of the Xishimen iron skarn deposit

Size (μm)	*T*vdisappear (°C)	*T*mNaCl (°C)	*T*mKCl (°C)	*C*NaCl (wt%)	*C*KCl (wt%)	Salinity (wt% NaCl equiv.)	Th (°C)	Comments
Type 2a fluid inclusion								
25	463	457	245	43.5	20.5	64.0		Not homogenized until heating to 800 °C
20	425	438	270	40.0	23.0	63.0		Not homogenized until heating to 800 °C
12	422	440	275	41.0	26.0	67.0		Decrepitated at 620 °C
10	483	495	230	52.0	13.0	65.0		Not homogenized until heating to 800 °C
14	426	480	290	48.0	20.0	68.0		Not homogenized until heating to 800 °C
10	445	450	305	39.0	30.0	69.0		Decrepitated at 510 °C
16	532	540	310	53.0	21.0	74.0		Not homogenized until heating to 800 °C
10	510	520	272	54.0	17.0	71.0		Not homogenized until heating to 800 °C
16	494	502	275	50.5	17.5	68.0		Not homogenized until heating to 800 °C
30	486	502	240	54.0	13.0	67.0		Decrepitated at 515 °C
10	542	578		70.8		70.8		Not homogenized until heating to 800 °C
20	542	575		70.4		70.4		Decrepitated at 570 °C
20	516	530		63.9		63.9		Not homogenized until heating to 800 °C
20	520	540		65.3		65.3		Not homogenized until heating to 800 °C
10	475	495		59.1		59.1		Not homogenized until heating to 800 °C
12	420	440		52.0		52.0		Decrepitated at 580 °C
10	412	435		51.4		51.4		Decrepitated at 570 °C
20	410	454		53.8		53.8		Decrepitated at 705 °C
10	470	495		59.1		59.1		Decrepitated at 600 °C
12	410	440		52.0		52.0		Decrepitated at 540 °C
20	476	495		59.1		59.1		Not homogenized until heating to 800 °C
8	464	500		59.8		59.8		Decrepitated at 560 °C
40	466	498		59.5		59.5		Not homogenized until heating to 800 °C
20	410	420		49.7		49.7		Not homogenized until heating to 800 °C
8	445	480		57.1		57.1		Not homogenized until heating to 800 °C
30	514	530		63.9		63.9		Not homogenized until heating to 800 °C
25	505	516		62.0		62.0		Not homogenized until heating to 800 °C
20	485	508		60.9		60.9		Not homogenized until heating to 800 °C
16	502	510		61.1		61.1		Not homogenized until heating to 800 °C
18	485	518		62.2		62.2		Not homogenized until heating to 800 °C
Type 2b fluid inclusion								
50	463	457	185	51.0	10.0	61.0	463	
40	410	416	226	42.0	17.0	59.0	416	
10	560	580	280	65.0	9.5	74.5	580	
12	408	421	210	47.0	18.0	65.0	421	
10	480	440	232	44.0	20.0	64.0	480	
20	540	553	238	68.0	2.5	70.5	553	
16	546	560	264	62.0	10.0	72.0	560	
30	517	460	205	49.5	12.0	61.5	517	
16	493	460		54.5		54.5	493	
12	505	525		63.2		63.2	525	
12	463	498		59.5		59.5	498	
16	465	495		59.1		59.1	495	
10	580	480		57.1		57.1	580	
16	620	475		56.4		56.4	620	

Table 1 (continued)

Size (μm)	*T*vdisappear (°C)	*T*mNaCl (°C)	*T*mKCl (°C)	*C*NaCl (wt%)	*C*KCl (wt%)	Salinity (wt% NaCl equiv.)	Th (°C)	Comments
20	580	350		42.4		42.4	580	
22	560	400		47.4		47.4	560	
16	572	585		71.8		71.8	585	
24	415	420		49.7		49.7	420	
10	580	498		59.5		59.	580	
12	462	478		56.8		56.8	478	
12	532	540		65.3		65.3	540	
8	520	538		65.0		65.0	538	
10	523	535		64.6		64.6	535	
10	560	576		70.5		70.5	576	
14	495	505		60.4		60.4	505	
16	580	535		64.6		64.6	580	
20	566	572		69.9		69.9	572	
20	440	454		53.8		53.8	454	
16	480	465		55.1		55.1	480	
20	480	445		52.6		52.6	480	
20	470	441		52.2		52.2	441	
10	470	495		59.1		59.1	495	
10	476	495		59.1		59.1	495	
30	462	508		60.9		60.9	508	
30	504	520		62.5		62.5	520	
24	512	532		64.2		64.2	532	
12	504	510		61.1		61.1	510	
8	488	506		60.6		60.6	506	
12	505	518		62.23		62.23	518	
6	492	508		60.85		60.85	508	
6	490	506		60.58		60.58	506	

Tvdisappear vapor disappearance temperature, *TmNaCl* melting temperature of NaCl, *TmKCl* melting temperature of KCl, *Th* total homogenization temperature, *CNaCl* concentration of NaCl, *CKCl* concentration of KCl

pyrrhotite crystal, $V_{\mathrm{HI}} * \rho_{\mathrm{HI}}$ represents the mass of halite crystal, and $V_{\mathrm{liquid}} * \rho_{\mathrm{liquid}}$ refers to the mass of aqueous phase. Pyrrhotite has a density of 4.65 g/cm^3 at room temperature and contains about 60 wt% Fe. The density of a NaC1-saturated solution at room temperature is ~1.2 g/cm^3 (Roedder 1971). With these parameters, the calculated iron concentrations in the fluid inclusions range from 1.02 to 8.45 wt%, with a mean of 4.08 wt% ($n = 13$; Table 2).

Sulfur isotopes

The sulfur isotopic compositions of pyrite from the iron ore bodies and calcite-pyrite veins are presented in Table 3. The $\delta^{34}S_{\text{V-CDT}}$ value of pyrite ranges from 14.0 to 18.6 ‰ (Fig. 12), with a mean of 16.2 ‰ ($n = 13$). The results are consistent with previous sulfur isotope data reported for Xishimen ($\delta^{34}S$ = 14.7–18.4 ‰; Li et al. 2013a).

Discussion

Nature and compositions of the ore-forming fluids

Opaque phases in fluid inclusions can be either trapped crystals or true daughter minerals precipitated from the ore-forming fluid; only true daughter minerals can be used as indicators for the composition and nature of the fluids (Kwak et al. 1986). The fact that pyrrhotite in the fluid inclusions did not dissolve during heating may imply that these crystals were trapped accidentally; the following observations and considerations, however, suggest

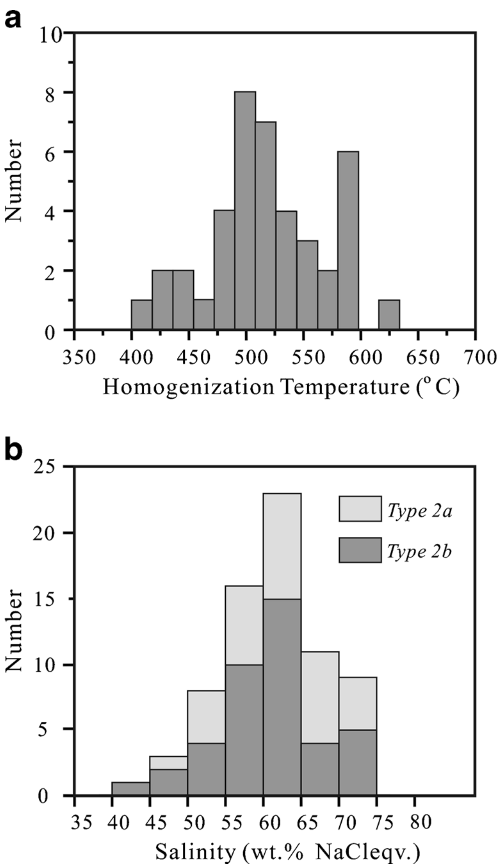

Fig. 8 Histograms of total homogenization temperatures and salinities of fluid inclusions

that they are true daughter minerals. Firstly, pyrrhotite-bearing fluid inclusions are widespread in both the rock-forming minerals (quartz and amphibole) of the ore-related diorite stock and skarn minerals (e.g., diopside). The universal presence and constant relative proportions of pyrrhotite in a large number of coeval fluid inclusions (Fig. 7a–d) indicate that this mineral was probably not trapped during crystal growth; rather, its occurrence is consistent with a primary origin. Secondly, pyrrhotite crystals typically coexist with halite and sylvite within a single fluid inclusion (Fig. 10a–d). This common intergrowth indicates that pyrrhotite and the salt minerals precipitated from the same fluid system. It is noted that the two-phase, vapor- or liquid-rich, salt-free fluid inclusions do not contain pyrrhotite, supporting our interpretation that this mineral was precipitated directly from a saline fluid. Lastly, neither the diorite stock nor the mineralized skarn assemblages contain pyrrhotite as a constituent mineral, ruling out the possibility that this mineral was a trapped phase. Taken together, we conclude that the pyrrhotite crystals are true daughter minerals. The failure of the pyrrhotite crystals to dissolve throughout the heating process may be due to post-entrapment diffusion of hydrogen from the inclusions, a process that could have led to an increase in fO_2 of the inclusions (Mavrogenes and Bodnar 1994), or due to leakage of the fluid inclusions during heating (Roedder 1984). Either increase in fO_2 or leakage of the fluid inclusions could have disabled dissolution of pyrrhotite (Reodder 1984). The morphological features of the fluid inclusions (Fig. 7), however, suggest that leakage is a less likely mechanism. Thus, hydrogen diffusion is the most likely mechanism leading to the resistant behavior of the pyrrhotite crystals throughout the heating process.

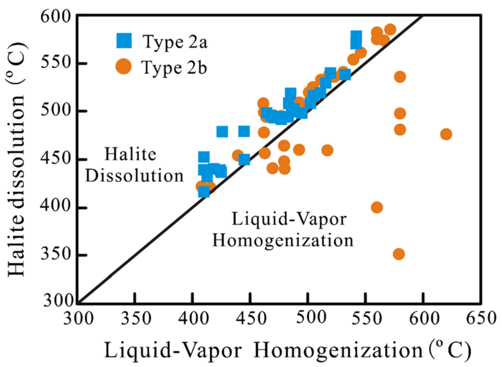

Fig. 9 Halite dissolution temperatures versus liquid-vapor homogenization temperatures for type 2a and type 2b fluid inclusions

The common occurrence of pyrrhotite-bearing fluid inclusions in both rock-forming minerals and prograde skarn minerals, together with the widespread halite and/or sylvite having or having no association with pyrrhotite, indicates that the magmatic hydrothermal fluids, which exsolved from a hydrous magma, were ferrous iron rich, saline to hyposaline, and reducing. The calculated iron concentrations of the studied fluid inclusions range from 1.02 to 8.45 wt%, comparable to values (1–9 wt%) of pyrite-bearing fluid inclusions from the Hole 16 W-Sn-F skarn deposit (Kwak et al. 1986). Higher iron concentrations would be expected for the fluid inclusions if ferrous iron dissolved in the liquid phase was considered. The high temperatures and high salinities of the fluids (Fig. 8) may explain their high iron concentrations. Whitney et al. (1985) experimentally demonstrated that iron concentrations in chloride solutions equilibrated with synthetic granite compositions are strongly affected by both temperature and salinity. They found that an increase in temperature from 400 to 500 °C caused a tenfold increase in iron concentration, with a maximum value being achieved at temperatures of 550 to 650 °C, consistent with the homogenization temperature of fluid inclusions investigated in this study (Fig. 8a). Because iron is largely complexed by chlorine in magmatic-hydrothermal fluids, increases in salinity (represented by NaCl wt% equivalent) have a profound effect in enhancing iron solubility and, therefore, its concentrations in the fluid. A threefold increase in salinity can compensate for a decrease in iron concentrations caused by decreasing the temperature from

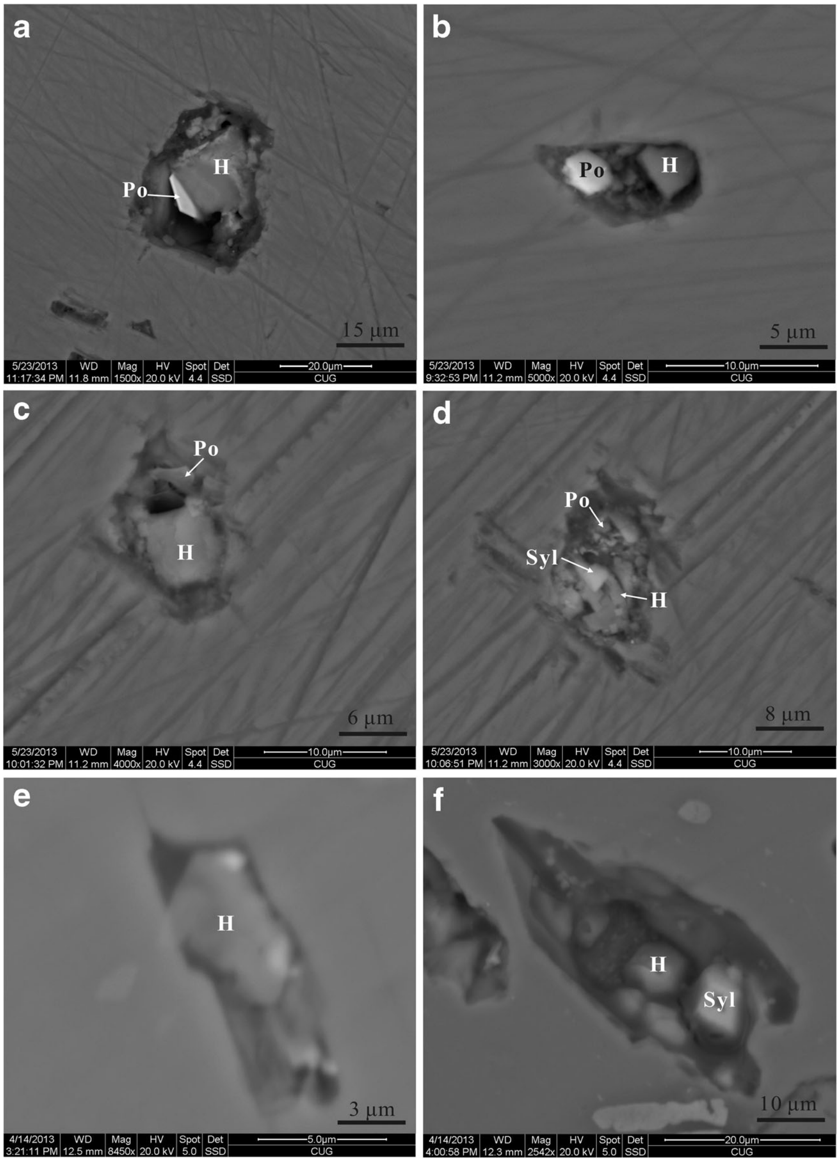

Fig. 10 SEM images of daughter minerals from exposed fluid inclusions. **a** Pyrrhotite crystal beneath halite. **b**, **c** Pyrrhotite crystals occurring beside a halite crystal. **d** Multiple halite crystals coexisting with a sylvite crystal and a pyrrhotite crystal. **e** Halite crystal with an irregular shape. **f** Cubic halite crystals and sylvite crystals. Mineral abbreviations as Figs. 5 and 6

600 to 400 °C (Whitney et al. 1985). These observations explain why iron sulfide minerals occur exclusively in fluid inclusions with high homogenization temperature (>420 to 620 °C) and high salinity (>51 to 74 wt% NaCl equiv) in the Xishimen iron skarn deposit.

Source of sulfur

The lack of sulfate minerals in the iron ores indicates that the sulfur isotopes of pyrite in the ores can be considered to approximate the isotopic compositions of the fluids ($\delta^{34}S_{\Sigma S}$) from which the ores precipitated (Zheng and Chen 2000). Pyrite from the Xishimen iron ores has $\delta^{34}S$ ranging from 14.0 to 18.6 ‰ (Table 3), much higher than values of magmatic sulfides from the ore-related diorite in the Wu'an magmatic belt (2.5–6.5 ‰ with a mean of 4.9 ‰; Zhang and Ma 1996) but comparable to isotopic compositions typical of marine sulfates (Seal et al. 2000). The middle Ordovician strata in the Handan-Xingtai district host numerous evaporite beds with a total thickness of 210 m (Cui 1983), which have $\delta^{34}S$ values of 24 to 29 ‰ with an average of 26 ‰ (Table 3). Evaporitic rocks are particularly abundant in the hanging wall of the main ore body of the Xishimen deposit (Fig. 4b). We therefore suggest that the sulfur in the evolving fluids was largely derived from the evaporites. Assuming that the original magmatic hydrothermal fluids degassed from the cooling magma had $\delta^{34}S$ values of 4.9 ‰ and that the evaporite-derived sulfur has an average $\delta^{34}S$ of 26 ‰, the mean $\delta^{34}S$ value (16.2 ‰) of pyrite from Xishimen can be explained by a mixture of 46 % magmatic sulfur and 54 % evaporite-derived sulfur.

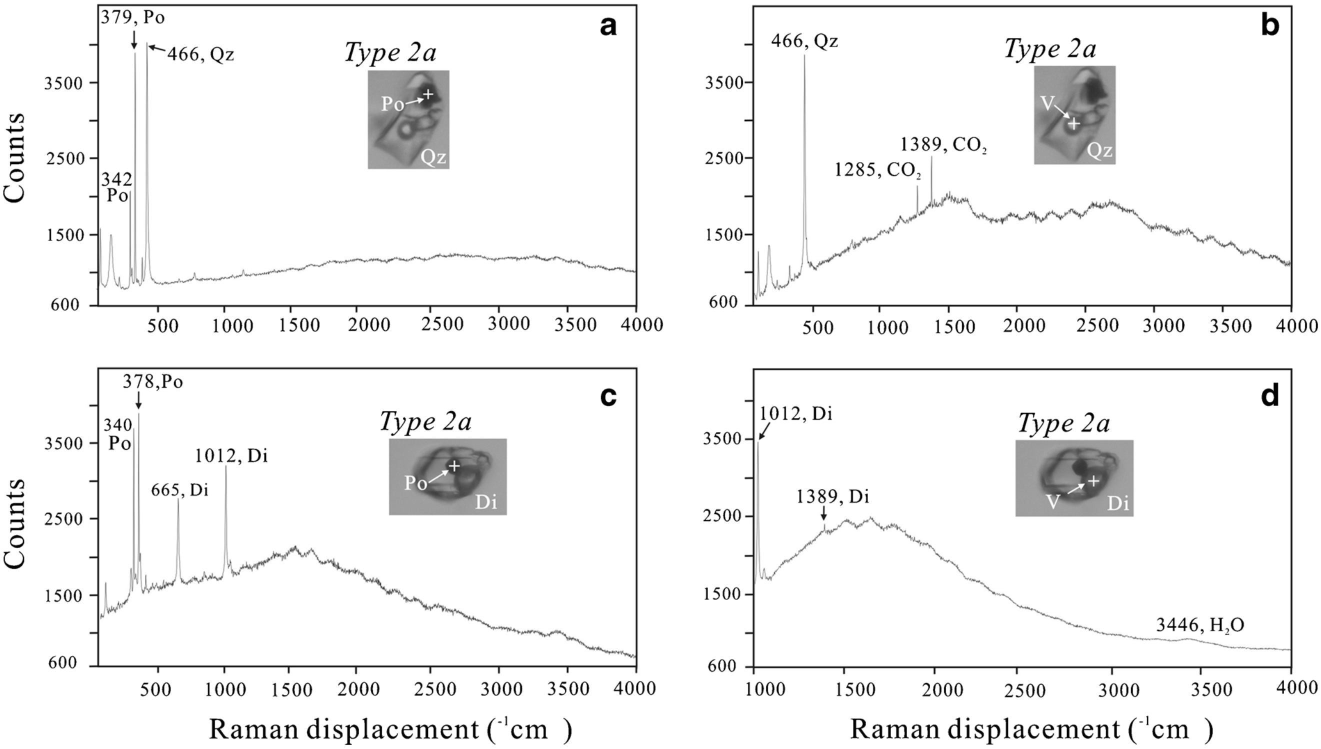

Fig. 11 Raman spectra of opaque mineral-bearing fluid inclusions in magmatic quartz (*Qz*) and hydrothermal diopside (*Di*). **a** Pyrrhotite as the most common opaque phase in type 2 inclusions in quartz from fresh diorite. **b** The vapor phase of type 2 inclusion in magmatic quartz is dominated by CO_2. **c** The opaque phase in type 2 inclusion in diopside from skarn is dominated by pyrrhotite. **d** The vapor phase of type 2 inclusion in diopside consists of H_2O and minor CO_2. Note that quartz and diopside are also detected in fluid inclusions hosted in these two minerals. Mineral abbreviations as Figs. 5 and 6

Table 2 Calculated iron concentrations of type 2 fluid inclusions in diopside of the Xishimen iron skarn deposit

Number	Phases										Iron concentration
	Pyrrhotite (ρ = 4.65 g/cm^3)		Halite (ρ = 2.17 g/cm^3)		Vapor	Liquid (ρ = 1.2 g/cm3)		*V*total	m_{total}		
	V (μm^3)	m (10^{-12} g)	V (μm^3)	m (10^{-12} g)	V (μm^3)	V (μm^3)	m (10^{-12} g)	V (μm^3)	m (10^{-12} g)		(wt%)
1	6.99	32.50	48.96	106.24	41.87	153.20	178.	251.01	316.99		6.15
2	78.35	364.33	956.44	2075.49	113.58	6424.31	7744.40	7572.69	10,184.21		2.15
3	29.69	138.06	185.19	401.87	63.59	840.55	984.90	1119.02	1524.83		5.43
4	55.62	258.63	318.75	691.69	193.85	916.58	1055.40	1484.80	2005.72		7.74
5	13.74	63.89	145.53	315.80	124.19	667.69	790.24	951.15	1169.93		3.28
6	61.19	284.53	521.21	1131.02	77.17	2289.54	2698.50	2949.11	4114.05		4.15
7	300.29	1396.35	2384.03	5173.35	623.15	7205.42	8406.27	10,512.89	14,975.97		5.59
8	7.58	35.25	373.25	809.95	646.74	782.02	932.36	1809.59	1777.55		1.19
9	34.96	162.56	357.91	776.67	62.32	860.44	1004.56	1315.63	1943.79		5.02
10	7.78	36.18	29.95	65.00	11.57	134.97	155.75	184.28	256.92		8.45
11	10.98	51.06	665.84	1444.87	555.85	1260.69	1504.04	2493.36	2999.97		1.02
12	1.92	8.93	64.00	138.88	38.14	252.41	301.35	356.47	449.16		1.19
13	47.04	218.74	1661.44	3605.33	935.09	3465.16	4120.55	6108.73	7944.62		1.65

ρ density, *V* volume, *m* mass

Table 3 Sulfur isotope data for pyrite and evaporite in the Handan-Xingtai district

Deposit/pluton	Sample description	Mineral	δ^{34}S (‰)	Reference
Xishimen deposit				
Sample XSM2-09	Magnitite ore	Pyrite	14.30	This study
Sample XSM2-12	Magnitite ore	Pyrite	14.90	
Sample XSM2-21	Magnitite ore	Pyrite	15.40	
Sample XSM2-01	Magnitite ore	Pyrite	14.00	
Sample XSM2-07	Magnitite ore	Pyrite	17.30	
Sample XSM-27	Magnitite ore	Pyrite	15.50	
Sample XSM-36	Magnitite ore	Pyrite	15.70	
Sample XSM-38	Magnitite ore	Pyrite	18.60	
Sample XSM-29	Magnitite ore	Pyrite	17.80	
Sample XSM-42	Magnitite ore	Pyrite	14.50	
Sample XSM-43	Magnitite ore	Pyrite	15.40	
Sample ZK18-1	Calcite-pyrite	Vein pyrite	18.50	
Sample ZK57-1	Calcite-pyrite	Vein pyrite	18.10	
	Magnitite ore	Pyrite	14.70	Li et al. (2013a)
	Magnitite ore	Pyrite	18.40	
Fushan deposit	Magnitite ore	Pyrite	12.1	Wang (2012)
	Magnitite ore	Pyrite	6.0	
	Magnitite ore	Pyrite	5.9	
	Magnitite ore	Pyrite	6.1	
	Magnitite ore	Pyrite	9.9	
Beiminghe deposit	Magnitite ore	Pyrite	13.5	Shen et al. (2012)
	Magnitite ore	Pyrite	13.7	
	Magnitite ore	Pyrite	12.2	
	Magnitite ore	Pyrite	14.4	
	Magnitite ore	Pyrite	16.5	
Beihe deposit	Magnitite ore	Pyrite	11.6	Zhang and Ma (1996)
	Magnitite ore	Pyrite	14.1	
	Magnitite ore	Pyrite	14.2	
Kuangshancun deposit	Magnitite ore	Pyrite	14.4	
Sibanpo deposit	Magnitite ore	Pyrite	14.7	
Er'lang deposit	Magnitite ore	Pyrite	15.2	
Jiangshan deposit	Magnitite ore	Pyrite	17.1	
	Magnitite ore	Pyrite	17.3	
Wujianzi deposit	Magnitite ore	Pyrite	17.2	
Taoshuwa deposit	Magnitite ore	Pyrite	17.7	
Xiaohezhai deposit	Magnitite ore	Pyrite	18.7	
Wu'an pluton	Diorite	Pyrite	6.5	
	Diorite	Pyrite	5.8	
	Diorite	Pyrite	2.5	
Wangyao deposit	Evaporite	Anhydrite	24.0	
	Evaporite	Anhydrite	25.1	
	Evaporite	Anhydrite	27.0	
	Evaporite	Anhydrite	29.1	

Mechanism of magnetite precipitation

Previous studies have shown that iron is present mainly in the ferrous state in magmatic-hydrothermal solutions (Crerar and Barnes 1976; Barnes 1979) and mostly forms ferrous chloride complexes (Holser and Schneer 1961; Chou and Eugster 1977; Eugster and Chou 1979; Kwak et al. 1986; Wood et al. 1987; Ulrich et al. 2001; Simon et al. 2013). Because

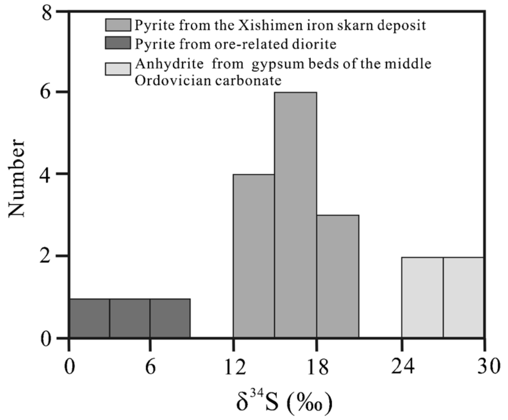

Fig. 12 Histogram of $\delta^{34}S$ of the sulfide minerals from the Handan-Xingtai district

two-third of the iron in magnetite is Fe^{3+}, the formation of magnetite from such fluids requires oxidation of significant amounts of Fe^{2+}. Fluid inclusion data confirm that the magmatic-hydrothermal fluids from which the Xishimen iron deposit formed had relatively low fO_2, with the iron being dominated by Fe^{2+} (Figs. 6, 7, 10, and 11). Cooling of such a reduced fluid would be unlikely to precipitate large amounts of magnetite or hematite; instead, the ferrous iron would be preferentially incorporated into silicates, iron sulfides, and siderite depending on the amount of silica, CO_2, and sulfur available in the fluids (Whitney et al. 1985).

In the Handan-Xingtai district, iron skarn deposits are closely related to the middle Ordovician evaporite-bearing carbonate strata, which host more than 95 % of the proven iron reserves of the district (Cai et al. 1987). The evaporitic beds, consisting mainly of gypsum, anhydrite, and halite, have a total thickness of a few hundred meters and form more than 30 economic gypsum and anhydrite deposits (Cai et al. 1987; Fig. 2). In sharp contrast, no economic iron deposits have been found in the Cambrian to early Ordovician carbonates or Carboniferous to Permian shales and sandstones where evaporites are lacking (Fig. 2). This observation indicates that the evaporitic rocks have played a critical role in the formation of the magnetite deposits.

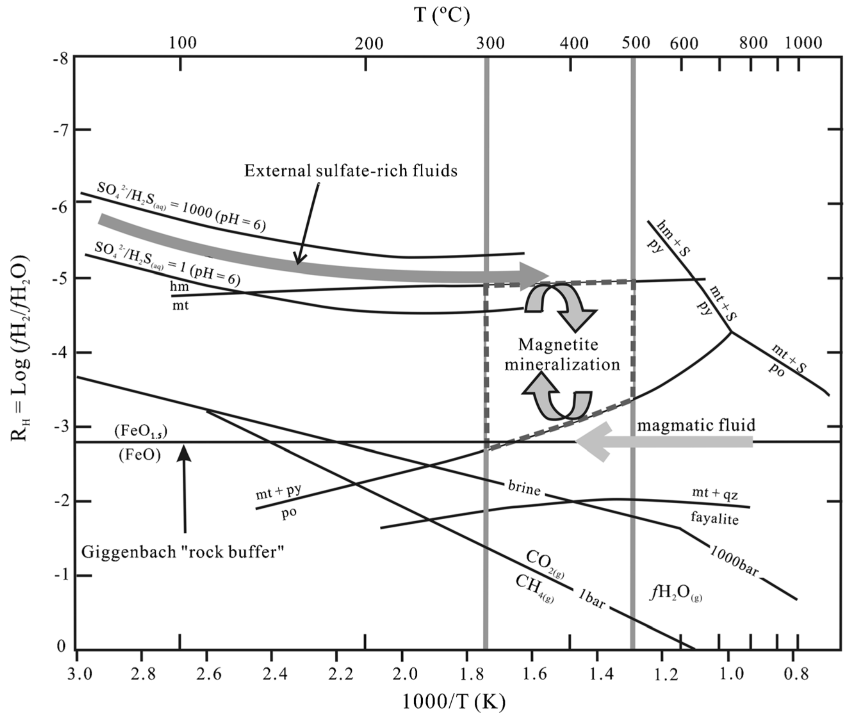

Fig. 13 R_H vs. 1000/T diagram showing the phase boundaries in the Fe-S-H_2O-CO_2-CH_4 fluid system (modified from Einaudi et al. 2003). Mineral reactions are calculated at 500 bar. The magnetite-hematite phase boundary was calculated from Myers and Eugster (1983) and is applicable for a temperature range of 25 to 670 °C. The "rock buffer" and CO_2-CH_4 buffer are from Giggenbach (1987). The temperature from 300 to 500 °C was set as the favorable conditions for magnetite precipitation based on fluid inclusion microthermometry. The *dark gray arrow* indicates the possible position of the evaporite-derived fluid with a high sulfate-sulfide ratio. The *light gray arrow* represents the possible position of the magmatic fluid. Due to fluid-rock interaction, the magmatic fluid exsolved from a subsolidus magma may follow the rock buffer line which lies generally below the magnetite-pyrite/pyrrhotite buffer line above 400 °C. This view is consistent with the observation that pyrrhotite commonly exists as a daughter mineral in fluid inclusions in igneous quartz, amphibole, and prograde skarn minerals (diopside in the present case). The CO_2-CH_4 buffer line is under the magnetite-pyrite/pyrrhotite buffer line above 300 °C and thus has little redox potential to control Fe-S mineralogy during magnetite mineralization. The ladder-shaped zone defined by *dashed lines* represents the area favorable for coprecipitation of magnetite and pyrite. Interaction between a reducing magmatic fluid and evaporite or mixing of the magmatic fluid with an evaporite-derived component may cause sudden changes in the redox state, leading to precipitation of magnetite and subsequently pyrite

This view is confirmed by a consistently high $\delta^{34}S$ value of pyrite from all iron deposits in the Handan-Xingtai district (5.9 to 18.7 ‰; Table 3).

Although $CaSO_4$ has very limited solubility in pure water (Morey and Hesselgesser 1951), an increase in X_{NaCl} in the hydrothermal fluid would significantly promote the solubility of $CaSO_4$ at high temperature and pressure (Newton and Manning 2005). For example, the solubility of $CaSO_4$ is about 0.4 mol in a NaCl-saturated solution at 500 °C and 10 kbar (Newton and Manning 2005). Formation water, basinal brine, or meteoric water that has sufficiently equilibrated with evaporites is commonly enriched in NaCl, enabling significant increases in sulfate in the solutions at high temperatures. These sulfate-rich fluids have high fO_2, generally above the sulfate-sulfide buffer in the R_H-1000/T diagram (Fig. 13; Giggenbach 1987; Einaudi et al. 2003), and thus are important oxidizing agents. The magmatic-hydrothermal fluids responsible for the Xishimen deposit were clearly reducing, as evidenced by the universal presence of pyrrhotite as a daughter mineral in fluid inclusions in both the rock-forming minerals of the diorite and the prograde skarn minerals (Figs. 6, 7, 10, and 11). Mixing of sulfate-rich, oxidizing fluids with ferrous iron-rich, reducing magmatic-hydrothermal fluids would trigger the deposition of magnetite under favorable temperature conditions (generally 300–500 °C), as illustrated by the following reaction (Figs. 13 and 14):

$$12Fe^{2+} + SO_4{}^{2-} + 12H_2O \leftrightharpoons 4Fe_3O_4 + H_2S + 22H^+ \qquad (1)$$

According to reaction (1), magnetite deposition is accompanied by a significant increase of H^+ in the fluids, which may suppress the formation of magnetite. Nevertheless, H^+ produced by reaction (1) would be effectively neutralized by reaction with the surrounding carbonate rocks, driving the reaction continuously toward the right. Consequently, large amounts of magnetite were likely precipitated to form the iron oxide ores.

The fO_2 of the ore-forming fluid would increase due to the following reactions (Einaudi et al. 2003; Pokrovski and Dubrovinsky 2011):

$$SO_4{}^{2-} + 2H^+ = H_2S + 2O_2 \qquad (2)$$

or

$$2H_2S + SO_4{}^{2-} + H^+ = S_3{}^- + 0.75O_2 + 2.5H_2O \qquad (3)$$

This suggests that hematite could form if the oxygen fugacity approaches the magnetite-hematite buffer. This view is confirmed by the widespread occurrence of hematite-magnetite ores in brecciaed marble, a few hundred meters

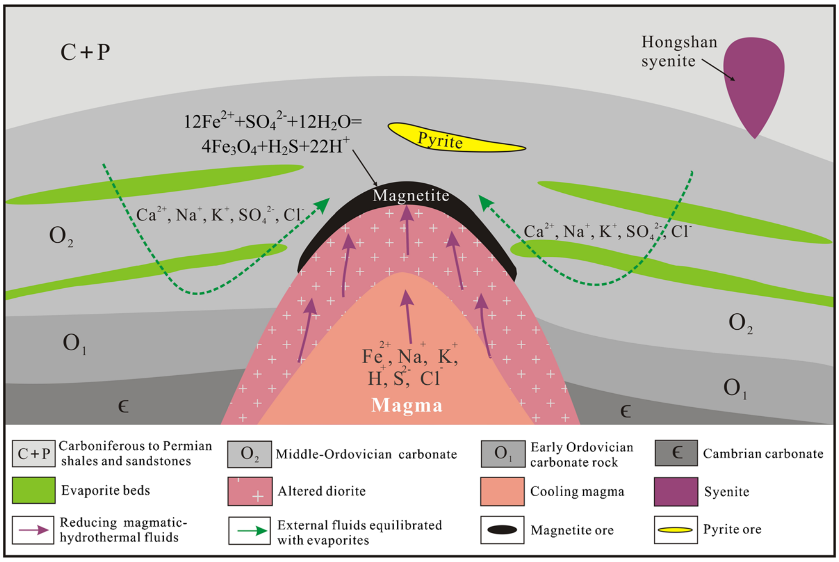

Fig. 14 A cartoon showing the evolution of ore-forming fluids in the iron skarn system of the Handan-Xingtai district. High-temperature, reducing, and Fe^{2+}-rich magmatic-hydrothermal fluids were exsolved from cooling magmas represented by the dioritic intrusions in the district. Within the contact zones between the magmatic intrusions and middle Ordovician evaporite-rich marine carbonate, the magmatic-hydrothermal fluids interacted with the evaporites or mixed with external fluid components that had equilibrated with the evaporite units, leading to precipitation of voluminous magnetite. Abundant pyrite formed as a result of the redox reactions, as represented by dense to sparse pyrite disseminations in the magnetite ores and massive aggregates and veins of pyrite in marble close to the intrusion. Lack of magnetite ores associated with the Hongshan syenite is best interpreted in terms of the paucity of evaporites in the Carboniferous and Permian strata in which the Hongshan syenite was emplaced (Fig. 1)

distant from the Xishimen diorite stock where evaporite beds are particularly abundant.

Oxidation-reduction reactions are common in most hydrothermal systems, mostly involving O, H, C, S, and Fe (Janecky et al. 1986). Laser Raman spectroscopic analysis indicates that H_2O and CO_2 (Fig. 11b, d) are the dominant components in the aqueous fluid inclusions and in the liquid phase of the daughter mineral-bearing fluid inclusions of the Xishimen deposit, without detectable CH_4 and H_2. Thus, ferrous iron was the only agent in the fluids capable of reducing evaporitic sulfates to form the observed iron oxides and sulfides (Fig. 13). Experimental studies of Cai (1984) provided additional evidence for magnetite precipitation via the redox reaction between sulfate and ferrous iron. His experiments were conducted at 550 to 250 °C and 500 to 100 bar with different oxygen fugacities, using 50 mg $CaSO_4 \cdot 2H_2O$ and 100 mg $FeCl_2 \cdot 4H_2O$ as the starting materials dissolved in 0.2–0.3-ml NaOH-H_2O solution. All experiments produced magnetite and minor amounts of iron sulfides. For example, the experiment conducted at 350 °C and 500 bar at the magnetite-quartz-fayalite (MQF) buffer yielded 22.96 mg of magnetite, 0.59 mg of pyrrhotite, and 0.88 mg of pyrite, together with H_2S.

Magnetite and pyrite are the predominant metallic minerals in the Xishimen iron skarn deposit. According to Evans (2006), the redox budget of a sample is defined as the number of moles of electrons that need to be added to the sample to reach the reference state. Thus, to form 1 mol of magnetite, 2 mol of ferrous iron needs to lose 2 mol of electrons, and to form 1 mol of pyrite, 2 mol of S^{6+} (sulfates as represented by gypsum and anhydrite in case of Xishimen) should gain 14 mol of electrons. To reach this charge balance, the molar ratio of magnetite to pyrite should be 7: 1, and the corresponding mass ratio of these two minerals should be 13.5:1. As discussed above, about 56 % of the sulfur in pyrite of the Xishimen deposit was derived from evaporitic sulfate; thus, the average ore grade of 43 % Fe in the deposit (HGI 1984) would correspond to 59.3 wt% magnetite, and the calculated sulfur content would be 4.3 wt% (S wt% = 64/120 $*$ Py wt%, Py wt% = 59.3/13.5/0.56 wt%). The calculated sulfur content is significantly higher than that contained in the iron ores (2 wt%; HGI 1984). This difference can be explained by the abundance of ^{34}S-enriched pyrite in the calcite-sulfide veins hosted in the marbles within a few hundred of meters of the ore bodies.

Implications for the genesis of iron oxide-dominated deposits

Many iron oxide ores, including skarn, iron oxide-apatite (IOA) and iron oxide-copper-gold (IOCG) deposits, have been shown to be closely related to evaporites, and many of them contain sulfide minerals that have $\delta^{34}S$ values significantly higher than those typical of magmatic sulfur (Table 4),

Table 4 Sulfur isotope data of sulfide minerals from selected iron oxide-dominated hydrothermal deposits

Types of ores	Region or district	$\delta^{34}S$ (‰)	Comments	Reference
Iron skarn	Handan-Xingtai, North China	6.0~18.7	Numerous evaporite beds in Ordovician carbonates	Zhang and Ma (1996); Li et al. (2013a, b)
Iron skarn	Linfen, North China	12.5~17.4	Numerous evaporite beds in Ordovician carbonates	Zhang et al. (2013a)
Iron skarn	Laiwu, North China	5.0~18.0	Numerous evaporite beds in Ordovician carbonates	Yuan (1982)
Iron skarn	Daye, South China	10.3~20	Abundant evaporites in Triassic carbonates	Zhu et al. (2013); Xie et al. (2015)
Iron skarn	Cornwall, USA	5.8~19.9	Possible evaporites or sulfate-bearing pore fluids	Rose et al. (1985)
Iron skarn	North Sweden	−7.9~24.7	Evidence for evaporites or seawater sulfate	Frietsch et al. (1995)
Iron skarn	Colima, Mexico	4.5~6.1	Possible evaporites or trapped seawater sulfate	Zürcher et al. (2001)
Iron skarn	Vegas Peladas, Argentina	No data	Extensive Jurassic evaporites	Pons et al. (2009)
IOA	Ningwu, China	−2.5~22.8	Abundant evaporites in Triassic sedimentary sequence	Li et al. (2014); Li et al. (2015)
IOA	Luzong, South China	−9.3~14.3	Abundant evaporites in Triassic sedimentary sequence	Li et al. (2014)
IOA	Bafq, Iran	−2.1~30	Extensive Cambrian and younger evaporites or seawater sulfate	Jami (2005)
IOA	Kiruna, Sweden	No data	Evidence for evaporites of rifting sequence	Hitzman et al. (1992)
IOCG	Kangdian, SW China	−3.8~15.9	Evaporites in Proterozoic rift sequence	Zhao and Zhou, (2011); Zhao (2010)
IOCG	Olympic Dam, Australia	−14~12.5	Possible involvement of metasedimentary sulfate or Proterozoic seawaters	Bastrakov et al. (2007) and references therein
IOCG	Mantoverde, Chile	−6.8~11.2	Evidence for incursion of modified seawater and evaporitic sediments	Benavides et al. (2007) and references therein
IOCG	Siberia, Russia	13.5–21	Evidence for evaporites	Vakhrushev et al. (1981)

indicating a likely external sulfur source (Barton and Johnson 1996, 2000; Chen 2013). Sulfides from iron skarn and IOA deposits in several major late Mesozoic iron districts in the NCC and adjacent regions (Fig. 1) are consistently characterized by unusually high $\delta^{34}S$ values of generally >10 ‰ (e.g., Yuan 1982; Zhang et al. 2013a; Li et al. 2014, 2015, Table 4). The best examples include the Laiwu, Linfen, Daye, Ningwu, and Luzong districts (Fig. 1). Iron skarn deposits from the Laiwu and Linfen districts are hosted in middle Ordovician, evaporite-bearing, carbonate strata. They share common mineralization and alteration features with iron skarn deposits in the Handan-Xingtai district and contain abundant sulfides with high $\delta^{34}S$ values (Cai 1981; Cai et al. 1987). For example, pyrite from the Pingshun iron skarn deposit in the Linfen district has $\delta^{34}S$ values of 12.5 to 17.4 ‰, which are interpreted to be a mixture of magmatic- and evaporite-derived sulfur (Zhang et al. 2013a). Major iron skarn deposits in the Daye district (e.g., Chengchao, Jinshandian) of the northeastern Yangtze craton are associated with Triassic evaporite-bearing sedimentary rocks and characterized by high $\delta^{34}S$ values of pyrite ranging from 10.3 to 20.0 ‰ (Xie et al. 2015), indicating a major contribution of external sulfur, most likely from the evaporites in the Triassic sequences (Zhu et al. 2013).

The Cornwall-type magnetite skarn deposit in Pennsylvania also shows significant ^{34}S enrichment in sulfides, with an average $\delta^{34}S$ of 11.4 ‰ (Rose et al. 1985). Heating and circulation of magmatic, meteoric, and sulfate-bearing connate waters or some combinations of these may have been responsible for the formation of the magnetite ores (Rose et al. 1985). Similarly, many iron skarn deposits in northern Sweden and western Mexico have sulfur isotopic signatures (e.g., $\delta^{34}S > 5$ ‰) indicating a mixture of magmatic-hydrothermal fluids and trapped seawater or evaporite-derived fluids during iron mineralization (Frietsch et al. 1995; Zürcher et al. 2001).

Iron oxide-apatite deposits in the Ningwu and Luzong volcanic basins, NE Yangtze craton (Fig. 1), are also related to Triassic evaporite-bearing, marine sedimentary units, which are underlain by a volcanic sequence (Li et al. 2014, 2015). High S/B and Ca/Na ratios revealed by in situ LA-ICP-MS analysis of fluid inclusions and heavy sulfur isotopic signatures of syn- and post-ore pyrite (up to 22.5 ‰ of $\delta^{34}S$; Table 4) from these two districts confirm a significant contribution from sedimentary sulfates (Li et al. 2015). Similarly, sulfides from many IOA deposits in central Iran (Bafq district) have very high $\delta^{34}S$ values (up to 30 ‰), confirming a significant input of seawater sulfate or evaporite-sourced sulfur during mineralization (Jami 2005). The IOCG deposits in the Kangdian region, western Yangtze craton (not shown in Fig. 1), mostly have positive $\delta^{34}S$ values (up to +15.9 ‰), a signature interpreted to reflect input of sulfur from evaporites in the Paleoproterozoic Yinmin Fm. (Zhao 2010; Zhao and Zhou 2011). High $\delta^{34}S$ values have also been reported for sulfides from many deposits of other major IOCG provinces, such as Olympic Dam (Australia), Mantoverde (Chile), and Siberia (Russia) (e.g., Vakhrushev et al. 1981; Bastrakov et al. 2007; Benavides et al. 2007, Table 4). The observed high $\delta^{34}S$ values in many of the world's IOCG deposits have been considered as indicating evaporite-sourced sulfur (Chen 2013). Collectively, we conclude that external sulfate, either from evaporites, basinal fluids, or seawater, could have played a critical role in the formation of iron oxide ore deposits by providing a major oxidizing agent.

Conclusions

Fluid inclusion data from the Xishimen iron skarn deposit show that the magnetite-dominated ores precipitated from high-temperature, high-salinity, and ferrous iron-rich reducing fluids that exsolved from a hydrous magma. Sulfur isotope data of pyrite in the ores indicate that evaporitic sulfates in the middle Ordovician marine carbonates provided a major source of sulfur in the ore fluids. The sulfates have acted as an important oxidant responsible for converting Fe^{2+} to Fe^{3+} to allow continuous precipitation of voluminous magnetite-dominated ores. The oxidation-reduction reaction between external sulfate and ferrous iron-dominated magmatic-hydrothermal fluids could have been a vital mechanism in the formation of the world's many iron oxide-dominated deposits such as iron skarn, IOCG, and IOA deposits.

Acknowledgments This research was financially supported by the Ministry of Science and Technology of China (2012CB416802) and National Natural Science Foundation of China (grants 41325007, 91414301, 91514303). We thank Jin Xiaoye, Li Yang, Wu Yaoqian, and Bai Ming for their help during the field work and Zhang Suxin and Zhang Yi for assistance in the SEM-EDS analysis. Prof. David Lentz (UNB) read an early version of the manuscript. Andreas Audétat, Michael Haschke, and an anonymous reviewer provided constructive reviews that have led to considerable improvement of presentation of the paper. Our thanks extend to Profs. Bernd Lehmann (Editor-in-Chief) and Shao-Yong Jiang (Associate Editor) for handling the manuscript.

References

Barnes HL (1979) Solubilities of ore minerals. In: Barnes HL (ed) Geochemistry of hydrothermal ore deposits, 2nd edn. Wiley, New York, pp. 404–460

Barton MD, Johnson DA (1996) Evaporitic-source model for igneous-related Fe oxide–(REE-Cu-Au-U) mineralization. Geology 24:259–262

Barton MD, Johnson DA (2000) Alternative brine sources for Fe-oxide (-Cu-Au) systems: implications for hydrothermal alteration and metals. In: Porter TM (ed) Hydrothermal iron oxide copper-gold and related deposits: a global perspective. PGC Publishing, Adelaide, pp. 43–60

Bastrakov EN, Skirrow RG, Davidson GJ (2007) Fluid evolution and origins of iron oxide Cu-Au prospects in the Olympic Dam district, Gawler Craton, South Australia. Econ Geol 102:1415–1440

Benavides J, Kyser TK, Clark AH, Oates CJ, Zamora R, Tarnovschi R, Castillo B (2007) The Mantoverde iron oxide-copper-gold district, III Región, Chile: the role of regionally derived, nonmagmatic fluids in chalcopyrite mineralization. Econ Geol 102:415–440

Cai BJ (1981) The conditions for the formation of the Daye-type iron ore deposits: the significance of evaporite beds for the formation of iron ore deposits. Bull Inst Geomech China Acad Geol Sci 1:110–118 in Chinese

Cai BJ, Li X, Wei S, Cui Y, He J (1987) Features of the middle Ordovician evaporates and its control over endogenic iron(sulfur) deposits in Han-Xing district, Hebei. Bull Inst Geomech China Acad Geol Sci 10:1–84 in Chinese

Cai YJ (1984) The experiments for transforming anhydrite to form reduced sulfur in high temperature solutions. Bull Nanjing Inst Geol Miner Res China Acad Geol Sci 5:36–53 in Chinese

Chen B, Tian W, Jahn BM, Chen ZC (2008) Zircon SHRIMP U–Pb ages and in-situ Hf isotopic analysis for the Mesozoic intrusions in South Taihang, North China craton: evidence for hybridization between mantle-derived magmas and crustal components. Lithos 102:118–137

Chen HY (2013) External sulphur in IOCG mineralization: implications on definition and classification of the IOCG clan. Ore Geol Rev 51:74–78

Chou IM, Eugster HP (1977) Solubility of magnetite in supercritical chloride solutions. Am J Sci 277:1296–1314

Crerar DA, Barnes HL (1976) Ore solution chemistry V. Solubilities of chalcopyrite and chalcocite assemblages in hydrothermal solution at 200 to 350 °C. Econ Geol 71:772–794

Cui YH (1983) The genesis of the breccia in the middle Ordovician strata from Han-Xing District. N China Inst J Hydroelectr Power 2:74–88 in Chinese

Deng XD, Li JW, Wen G (2015) U-Pb geochronology of hydrothermal zircons from the Early Cretaceous iron skarn deposits in the Handan-Xingtai District, North China Craton. Econ Geol 110: 2159–2180

Einaudi MT (1981) Skarn deposits. Econ Geol 75:317–391

Einaudi MT, Hedenquist JW, Inan EE (2003) Sulfidation state of fluids in active and extinct hydrothermal systems: transitions from porphyry to epithermal environments. Soc Econ Geol Spec Publ 10:285–313

Eugster HP, Chou IM (1979) A model for the deposition of Cornwall-type magnetite deposits. Econ Geol 74:763–774

Evans KA (2006) Redox decoupling and redox budgets: conceptual tools for the study of earth systems. Geology 34:489–492

Frietsch R, Billström K, Perdahl J (1995) Sulphur isotopes in Lower Proterozoic iron and sulphide ores in northern Sweden. Mineral Deposita 30:275–284

Giggenbach WF (1987) Redox processes governing the chemistry of fumarolic gas discharges from White Island, New Zealand. Appl Geochem 2:143–161

HGI (Hebei Geological Institute) (1984) Regional geology survey report (ore deposits part), Unpublished exploration report, Hebei, pp 85 (in Chinese)

IGSNC (Institute of Geological Sciences of North China) (1976) Hanxing-type iron ore deposits in the Taihang Mountain areas. Unpublished exploration report, Hebei, pp 154 (in Chinese)

Hitzman MW (2000) Iron oxide-Cu-Au deposits: what, where, when, and why. In: Porter TM (ed) Hydrothermal iron oxide copper-gold and related deposits: a global perspective. PGC Publishing, Adelaide, pp. 9–25

Hitzman MW, Oreskes N, Einaudi MT (1992) Geological characteristics and tectonic setting of Proterozoic iron oxide (Cu-U-Au-REE) deposits. Precambrian Res 58:241–287

Holser WT, Schneer CJ (1961) Hydrothermal magnetite. Geol Soc Am Bull 72:369–385

Hu H, Li JW, Lentz D, Ren Z, Zhao XF, Deng XD, Hall D (2014) Dissolution–reprecipitation process of magnetite from the Chengchao iron deposit: insights into ore genesis and implication for in-situ chemical analysis of magnetite. Ore Geol Rev 57:393–405

Jami, M (2005) Geology, geochemistry and evolution of the Esfordi phosphate-iron deposit, Bafq area, Central Iran Ph.D. Thesis. University of New South Wales, Sydney

Janecky DR, Seyfried WE, Berndt ME (1986) Fe-O-S redox reactions and kinetics in hydrothermal systems. 5th international meeting on water-rock interaction, Reykjavik, Iceland: 1–4

Jin Z, Zhang Z, Hou T, Santosh M, Han L (2015) Genetic relationship of high-Mg dioritic pluton to iron mineralization: a case study from the Jinling skarn-type iron deposit in the North China Craton. J Asian Earth Sci 113:957–979

Kwak T, Brown WM, Abeysinghe PB, Tan TH (1986) Fe solubilities in very saline hydrothermal fluids: their relation to zoning in some ore deposits. Econ Geol 81:447–465

Li JW, Bi SJ, Selby D, Chen L, Vasconcelos P, Thiede D, Zhou MF, Zhao XF, Li ZK, Qiu HL (2012) Giant Mesozoic gold provinces related to the destruction of the North China craton. Earth Planet Sci Lett 349: 26–37

Li SR, Santosh M, Zhang H, Shen JF, Dong G, Wang J, Zhang J (2013a) Inhomogeneous lithospheric thinning in the central North China Craton: zircon U–Pb and S–He–Ar isotopic record from magmatism and metallogeny in the Taihang Mountains. Gondwana Res 23:141–160

Li WT, Audétat A, Zhang J (2015) The role of evaporites in the formation of magnetite–apatite deposits along the Middle and Lower Yangtze River, China: evidence from LA-ICP-MS analysis of fluid inclusions. Ore Geol Rev 67:264–278

Li YH, Duan C, Han D, Chen XW, Wang CL, Yang BY, Zhang C, Liu F (2014) Effect of sulfate evaporate salt layer for formation of porphyrite iron ores in the Middle-Lower Yangtze River area. Acta Petrol Sin 30:1355–1368 in Chinese with English abstract

Li YH, Xie GQ, Duan C, Han D, Wang CL (2013b) Effect of sulfate evaporate salt layer over the formation of skarn-type iron ore. Acta Geol Sin 87:1324–1334 in Chinese with English abstract

Mavrogenes JA, Bodnar RJ (1994) Hydrogen movement into and out of fluid inclusions in quartz: experimental evidence and geologic implications. Geochim Cosmochim Acta 58:141–148

Meinert LD (1984) Mineralogy and petrology of iron skarns in western British Columbia, Canada. Econ Geol 79:869–882

Meinert LD (1995) Compositional variation of igneous rocks associated with skarn deposits-chemical evidence for a genetic connection between petrogenesis and mineralization. Mineral Assoc Can Short Course Ser 23:401–418

Meinert LD, Dipple GM, Nicolescu S (2005) World skarn deposits. Econ Geol 100th Anniversary Volume:299–336

Metzger FW, Kelly WC, Nesbitt BE, Essene EJ (1977) Scanning electron microscopy of daughter minerals in fluid inclusions. Econ Geol 72:141–152

Morey GW, Hesselgesser JM (1951) The solubility of some minerals in superheated steam at high pressures. Econ Geol 46:821–835

Myers JT, Eugster HP (1983) The system Fe-Si-O: Oxygen buffer calibrations to 1,500 K. Contrib Mineral Petr 82:75–90

Newton RC, Manning CE (2005) Solubility of anhydrite, CaSO4, in NaCl–H2O solutions at high pressures and temperatures:applications to fluid–rock interaction. J Petrol 46:701–716

Peng TP, Wang YJ, Fan WM, Guo F, Peng BX (2004) SHRIMP zircon U-Pb geochronology of the diorites for southern Taihang Mountains in the North China interior and its petrogenesis. Acta Petrol Sin 20: 1253–1262 in Chinese with English abstract

Pokrovski GS, Dubrovinsky LS (2011) The S_3^- ion is stable in geological fluids at elevated temperatures and pressures. Science 331:1052–1054

Pons JM, Franchini M, Meinert L, Recio C, Etcheverry R (2009) Iron skarns of the Vegas Peladas District, Mendoza, Argentina. Econ Geol 104:157–184

Reodder E (1984) Fluid inclusions. Rev Mineral 12:644

Roedder E (1971) Fluid inclusion studies on the porphyry-type ore deposits at Bingham, Utah, Butte, Montana, and Climax, Colorado. Econ Geol 66:98–118

Rose AW, Herrick DC, Deines P (1985) An oxygen and sulfur isotope study of skarn-type magnetite deposits of the Cornwall type, southeastern Pennsylvania. Econ Geol 80:418–443

Seal RR, Alpers CN, Rye RO (2000) Stable isotope systematics of sulfate minerals. Rev Mineral Geochem 40:541–602

Shen JF, Santosh M, Li SR, Zhang H, Yin N, Dong G, Wang Y, Ma G, Yu H (2012) The Beiminghe skarn iron deposit, eastern China: geochronology, isotope geochemistry and implications for the destruction of the North China Craton. Lithos 156-159:218–229

Simon A, Bilenker L, Bell A (2013) The importance of iron mobility in magmatic-hydrothermal systems. Mineral Mag 77:2215

Sterner SM, Hall DL, Bodnar RJ (1988) Synthetic fluid inclusions. V. Solubility relations in the system NaCl-KCl-H_2O under vapor-saturated conditions. Geochim Cosmochim Acta 52:989–1005

Sun Y, Xiao L, Zhu D, Wu T, Deng XD, Bai M, Wen G (2014) Geochemical, geochronological, and Sr–Nd–Hf isotopic constraints on the petrogenesis of the Qicun intrusive complex from the Handan–Xingtai district: implications for the mechanism of lithospheric thinning of the North China Craton. Ore Geol Rev 57:363–374

Takagi T, Tsukimura K (1997) Genesis of oxidized-and reduced-type granites. Econ Geol 92:81–86

Ulrich T, Günther D, Heinrich CA (2001) The evolution of a porphyry Cu-Au deposit, based on LA-ICP-MS analysis of fluid inclusions: Bajo de la Alumbrera, Argentina. Econ Geol 96:1743–1774

Vakhrushev V, Ripp G, Kaviladze M (1981) Isotope composition of sulfur from iron ore deposits of East Siberia. Geol Geofiz 22:74–81

Wang, YJ (2012) The characteristics of Fushan iron deposit, Handan, Hebei province, China, and its implication to the North China Craton evolution. M.S. Thesis. China University of Geosciences, Beijing (in Chinese with English abstract)

Wei, HF (2011) Geological Characteristics and Genesis of Xishimen Skarn Iron deposit in Handan-Xingtai District. M.S. Thesis. Shijiazhuang University of Economics, Shijiazhuang (in Chinese with English abstract)

Whitney JA, Hemley JJ, Simon FO (1985) The concentration of iron in chloride solutions equilibrated with synthetic granitic compositions: the sulfur-free system. Econ Geol 80:444–460

Wood SA, Crerar DA, Borcsik MP (1987) Solubility of the assemblage pyrite-pyrrhotite-magnetite-sphalerite-galena-gold-stibnite-bismuthinite-argentite-molybdenite in H_2O-NaCl-CO_2 solutions from 200 to 350 °C. Econ Geol 82:1864–1887

Xie GQ, Mao JW, Zhu QQ, Yao L, Li YH, Li W, Zhao HJ (2015) Geochemical constraints on Cu–Fe and Fe skarn deposits in the Edong district, Middle–Lower Yangtze River metallogenic belt, China. Ore Geol Rev 64:425–444

Yang Z, Cheng Y, Wang H (1986) The geology of China. Oxford University Press, New York, p. 306

Yuan WL (1982) Ore genesis of Jinling iron skarn deposit based on sulfur isotope analysis. J Inst Met 1 :–139in Chinese

Zhang BM, Ma G (1996) Magmatism associated metal series and metallogenic model of the main metallogenic zones in Hebei. J Geol Min Res N China 11:351–360 in Chinese

Zhang HD, Liu JC, Peng SX, Zhang S, Men WH, Wang RM, JL W, Huang SW (2013a) Ore-forming material sources of the Pingshun iron deposits in the southern Taihang Mountains: constraints from trace elements and S and Pb isotopes. Geol Explor 6:1088–1097 in Chinese with English abstract

Zhang JQ, Li SR, Wang J, Bai M, Lu J, Wei H, Nie X, Liu H (2013b) The genetic mineralogical study of magnetite in Baijian and Xishimen skarn type of iron deposit, southern Hebei province. Earth Sci Front 20:76–87 in Chinese with English abstract

Zhao, XF (2010) Paleoproterozoic crustal evolution and Fe-Cu metallogeny of the western Yangtze Block, SW China Ph.D. Thesis. The University of Hong Kong, Hong Kong

Zhao XF, Zhou MF (2011) Fe–Cu deposits in the Kangdian region, SW China: a Proterozoic IOCG (iron-oxide–copper–gold) metallogenic province. Mineral Deposita 46:731–747

Zhao GC, Sun M, Wilde SA, Sanzhong L (2005) Late Archean to Paleoproterozoic evolution of the North China craton: key issues revisited. Precambrian Res 136:177–202

Zhao YM, Lin W, Bi C, Li D, Jiang C (1990) Skarn deposits of China. Geological Press, Beijing in Chinese

Zheng, JM (2007) The ore-forming fluid and mineralization of skarn Fe deposits in Handan-Xingtai area, south Hebei Ph.D. Thesis. China University of Geosciences, Beijing (in Chinese with English abstract)

Zheng JM, Xie GQ, Liu J, Chen M, Wang S, Guo S, Gao X, Li G (2007) $^{40}Ar/^{39}Ar$ dating of phlogopite from the Xishimen skarn iron deposit in the Handan-Xingtai area, southern Hebei, and its implication. Acta Petrol Sin 23:2513–2518 in Chinese with English abstract

Zheng YF, Chen JF (2000) Geochemistry of stable isotopes. Science Press, Beijing in Chinese

Zhu QQ, Xie GQ, Wang J, Li W, Yu B (2013) The relationship between the evaporate and skarn-type iron deposit: a case study of the Jinshandian iron skarn deposit in Hubei. Acta Geol Sin 87:1419–1428 in Chinese with English abstract

Zürcher L, Ruiz J, Barton MD (2001) Paragenesis, elemental distribution, and stable isotopes at the Peña Colorada iron skarn, Colima, Mexico. Econ Geol 96:535–557